

Electronic structure reconstruction by orbital symmetry breaking in IrTe₂

D. Ootsuki¹, S. Pyon², K. Kudo², M. Nohara², M. Horio³, T. Yoshida³, A. Fujimori³, M. Arita⁴, H. Anzai⁴, H. Namatame⁴, M. Taniguchi^{4,5}, N. L. Saini^{6,1}, and T. Mizokawa¹

¹*Department of Complexity Science and Engineering & Department of Physics, University of Tokyo, 5-1-5 Kashiwanoha, Chiba 277-8561, Japan*

²*Department of Physics, Okayama University, Kita-ku, Okayama 700-8530, Japan*

³*Department of Physics, University of Tokyo, 7-3-1 Hongo, Tokyo 113-0033, Japan*

⁴*Hiroshima Synchrotron Radiation Center, Hiroshima University, Higashi-hiroshima 739-0046, Japan*

⁵*Graduate School of Science, Hiroshima University, Higashi-hiroshima 739-8526, Japan and*

⁶*Department of Physics, University of Roma "La Sapienza" Piazzale Aldo Moro 2, 00185 Roma, Italy*

(Dated: November 19, 2018)

We report an angle-resolved photoemission spectroscopy (ARPES) study on IrTe₂ which exhibits an interesting lattice distortion below 270 K and becomes triangular lattice superconductors by suppressing the distortion via chemical substitution or intercalation. ARPES results at 300 K show multi-band Fermi surfaces with six-fold symmetry which are basically consistent with band structure calculations. At 20 K in the distorted phase, topology of the inner Fermi surfaces is strongly modified by the lattice distortion. The Fermi surface reconstruction by the distortion depends on the orbital character of the Fermi surfaces, suggesting importance of Ir 5*d* and/or Te 5*p* orbital symmetry breaking.

PACS numbers: 74.70.Xa, 74.25.Jb, 71.30.+h, 71.20.-b

Transition-metal compounds with multi-band Fermi surfaces often exhibit rich and interesting physical properties such as spin-charge-orbital order and superconductivity which originate from the topology of their multi-band Fermi surfaces. For example, the multi-orbital electronic structures of transition-metal oxides and chalcogenides including CuIr₂S₄ and Ca_{2-x}Sr_xRuO₄ provide various metal-insulator transitions with spin-charge-orbital ordering [1–4]. Also the multi-band structure of the Fe 3*d* orbitals play important roles in superconductivity and magnetism of Fe pnictides and chalcogenides such as LaFeAsO_{1-x}F_x [5]. Recently, Pyon *et al.* [6] and Yang *et al.* [7] have discovered interesting interplay between lattice distortion and superconductivity in triangular lattice IrTe₂ in which multi-band Fermi surfaces are expected to play significant roles. Since the large spin-orbit interaction of Ir 5*d* electrons is expected to entangle the spin and orbital degrees of freedom in IrTe₂ and the derived superconductors, Yang *et al.* pointed out that the IrTe₂ system provides a new playground to explore and/or realize topological quantum states, which are currently attracting great interest in physics community [7].

IrTe₂ exhibits a structural phase transition at ~ 270 K from the trigonal (P3m-1) to the monoclinic (C2/m) structure accompanied by anomalies of electrical resistivity and magnetic susceptibility [8]. When the lattice distortion is suppressed by chemical substitution of Pt or Pd for Ir or intercalation of Pd, IrTe₂ becomes superconductors [6, 7]. An electron diffraction study by Yang *et al.* [7] observed the superlattice peaks with wave vector of $q = (1/5, 0, -1/5)$ below the structural transition temperature. Such superstructure can be explained by charge density wave (CDW) driven by perfect or par-

tial nesting of multi-band Fermi surfaces. In multi-band Fermi surfaces derived from Ir 5*d* and Te 5*p* orbitals, the nesting character can be enhanced by orbitally-induced Peierls mechanism [9]. In addition, charge modulation of Ir 5*d* electrons is indicated by an Ir 4*f* x-ray photoemission study [10]. On the other hand, a recent optical study by Fang *et al.* on single crystal samples shows that there is no gap opening expected for CDW and, instead, band structure is reconstructed over a broad energy scale up to ~ 2 eV [11]. Fang *et al.* conclude that the structural transition of IrTe₂ is not of CDW type but of a novel type driven by Te 5*p* holes [11].

In this context, it is very interesting and important to study the geometry of multi-band Fermi surfaces of IrTe₂ using angle-resolved photoemission spectroscopy (ARPES). In the present ARPES study, above the transition temperature, the flower-shaped outer Fermi surface and the inner Fermi surfaces like six connected beads, which are predicted by band structure calculations, are partly identified. Across the structural transition, the topology of the inner Fermi surfaces is modified more strongly than that of the outer Fermi surface. Below the transition temperature, the inner Fermi surfaces consist of two straight portions, suggesting Fermi surface nesting. However, clear gap opening expected for CDW is not observed in the ARPES spectra, consistent with the optical study [11]. Instead, spectral weight is partially suppressed at specific points of the straight Fermi surfaces.

Single crystal samples of IrTe₂ were prepared using a self-flux method [11, 12]. The ARPES measurements were carried out at beamline 9A, Hiroshima Synchrotron Radiation Center using a SCIENTA R4000 analyzer with circularly polarized light of photon energy $h\nu = 23$ eV.

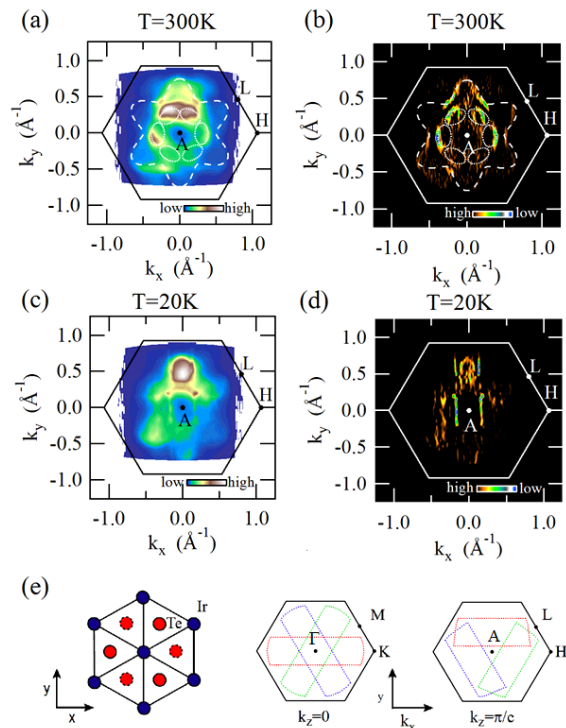


FIG. 1: (color online) (a) Fermi surface map and (b) its second derivative map of IrTe₂ for $h\nu = 23$ eV taken at 300 K. (c) Fermi surface map and (d) its second derivative map of IrTe₂ for $h\nu = 23$ eV taken at 20 K. The integration energy window of ± 5 meV at the Fermi level (E_F). The center of the hexagon roughly corresponds to the A point for $h\nu = 23$ eV. For 300 K, the flower-shaped outer Fermi surface and the inner Fermi surfaces with six-fold symmetry are schematically shown by the dashed and dotted curves, respectively. (e) Schematic drawings for the Ir triangular lattice and the hexagonal Brillouin zone at $k_z = 0$ and $k_z = \pi/c$. The Te ions indicated by solid (dotted) circles are located above (below) the Ir plane. The thin solid curves indicate possible Brillouin zone boundaries for possible three domains considering the superstructure reported in ref. 7.

The data were collected at 300 K and 20 K with an angular resolutions of $\sim 0.3^\circ$ and energy resolution of 18 meV for excitation energy of $h\nu = 23$ eV. The incident beam is 50° off the sample surface. The base pressure of the spectrometer was in the 10^{-9} Pa range. The samples were cleaved at 300 K under the ultrahigh vacuum and cooled across the structural transition, and then warmed to 300 K to check the reproducibility at 300 K. The samples were oriented by *ex situ* Laue measurements. The spectra were acquired within 8 hours after the cleavage. Binding energies were calibrated using the Fermi edge of gold reference samples.

The Fermi surface mapping of IrTe₂ measured at 300 K above the structural transition temperature are displayed in Figure 1(a). At $h\nu = 23$ eV, the momentum perpendicular to the Ir plane approximately corresponds to π/c , where c is the out-of-plane lattice constant, and

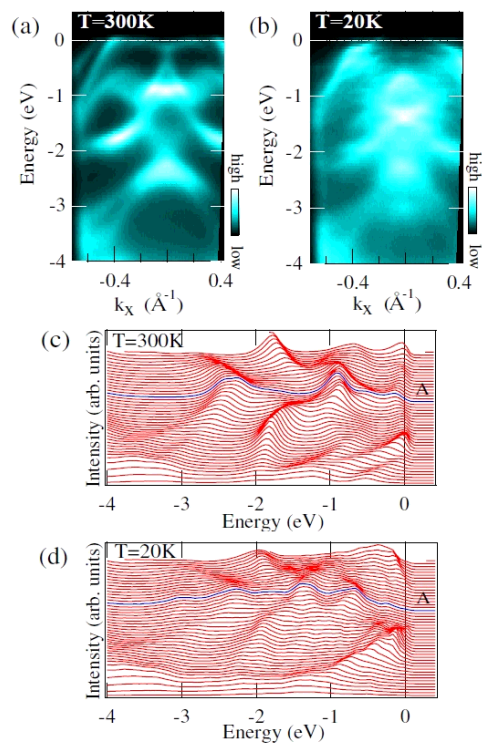


FIG. 2: (color online) Broad-range band dispersions along the A-H direction of IrTe₂ for $h\nu = 23$ eV taken at 300 K (a) and at 20 K (b). Broad-range energy distribution curves along the A-H direction of IrTe₂ for $h\nu = 23$ eV taken at 300 K (c) and at 20 K (d).

the center of the hexagonal Brillouin zone is the A point. The direction from the A point to the L (H) point corresponds to the direction of Ir-Ir (Ir-Te) bond. In Figs. 1(a), several Fermi surfaces can be identified as predicted by the band structure calculations [7, 11] although the strong intensity asymmetry due to transition-matrix element effect does not allow perfect identification. In order to extract the shapes of the Fermi surfaces, the second derivative along the cut direction $d^2I(k_x, k_y)/d^2k_x$ is plotted in Fig. 1(b). The flower shape for the outer Fermi surface is more clearly seen which is schematically indicated by the dashed curve. In addition, the inner Fermi surfaces like six connected beads can be identified as indicated by the dotted curves although effect of thermal excitations at 300 K tends to obscure the relatively small Fermi pockets. The inner Fermi surfaces observed around the A point at 300 K are roughly consistent with the prediction of band-structure calculations [7, 11].

Figure 1(c) shows the Fermi surface mapping at 20 K well below the transition temperature. Across the structural transition, in the region where the outer Fermi surface is close to the inner Fermi surfaces, while the outer Fermi surface at 300 K is observed separately from the inner Fermi surfaces, the outer Fermi surface at 20 K disappears due to partial gap opening or overlaps with

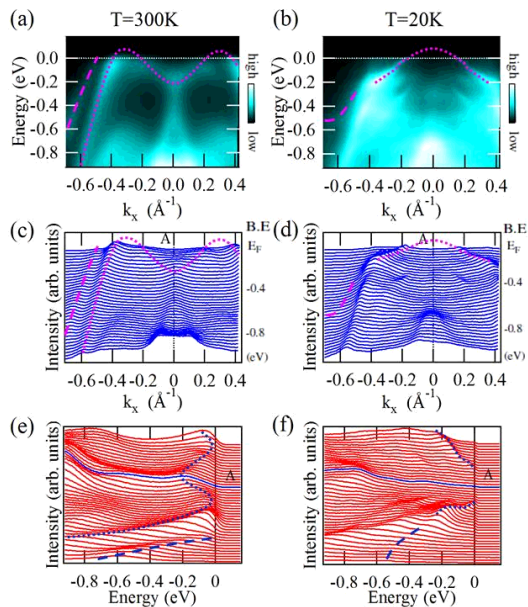


FIG. 3: (color online) Near- E_F band dispersions along the A-H direction of IrTe₂ for $h\nu = 23$ eV taken at 300 K (a) and at 20 K (b). Near- E_F momentum distribution curves along the A-H direction of IrTe₂ for $h\nu = 23$ eV taken at 300 K (c) and at 20 K (d). Near- E_F energy distribution curves along the A-H direction of IrTe₂ for $h\nu = 23$ eV taken at 300 K (e) and at 20 K (f). The outer hole bands and the inner hole-like bands are indicated by the dashed and dotted curves, respectively.

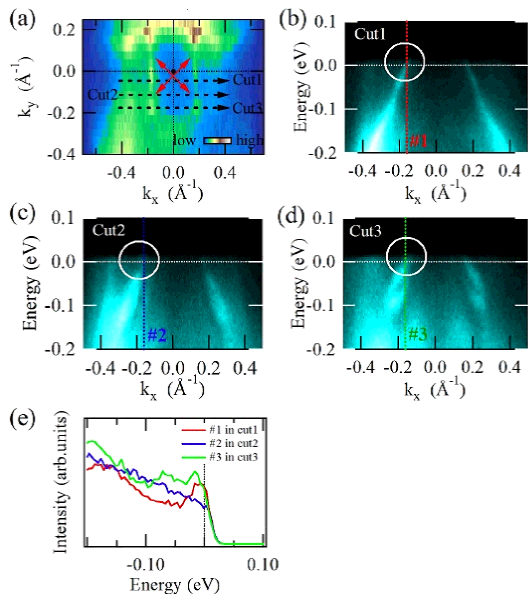


FIG. 4: (color online) (a) Fermi surface mapping near the A point at 20 K for $h\nu = 23$ eV. (b-d) Near- E_F band dispersions along the cuts parallel to the A-H direction at 20 K for $h\nu = 23$ eV. (e) Near- E_F energy distribution curves at the selected Fermi surface points at 20 K.

the inner Fermi surfaces. In addition, in going from 300 K to 20 K, intensity evolves in the six leaves of the outer Fermi surface flower probably due to band folding with $q = (1/5, 0, -1/5)$. In contrast to the limited effect on the outer Fermi surface, the inner Fermi surfaces dramatically change their shapes by the structural transition. The band structure calculations show that the outer Fermi surface is mainly constructed from the Ir $5d a_{1g}$ [$\frac{1}{\sqrt{3}}(XY + YZ + ZX)$] and Te $5p_z$ orbitals, and that the inner Fermi surfaces mainly have the Ir $5d e'_g$ [$\frac{1}{\sqrt{3}}(XY + e^{\pm 2\pi i/3}YZ + e^{\pm 4\pi i/3}ZX)$] and Te $5p_{x,y}$ orbital components (Here, the X-, Y-, and Z-axes are along the three Ir-Te bonds of a regular IrTe₆ octahedron). This assignment is supported by the good agreement between the ARPES result at 300 K and the band structure calculations [7, 11]. As for the band structure change across the transition, the experimental result that the inner Fermi surfaces are more strongly affected by the transition is consistent with the band structure calculation by Fang *et al* [11]. However, the geometry of inner Fermi surfaces at 20 K deviates from the prediction of the calculation. Interestingly, two straight portions of Fermi surfaces are observed at 20 K. The straight portions are perpendicular to the A-H direction or the direction of Ir-Te bond. Therefore, both of the Te $5p$ and Ir $5d$ orbitals would be involved in the structural transition if the straight Fermi surfaces are driven by orbitally-induced Peierls mechanism [9].

Figures 2(a) and (b) show the broad-range band dispersions along the A-H direction at 300 K and 20 K, respectively. Whereas the broad-range band dispersions at 300 K roughly agree with the predictions of the band-structure calculations, those at 20 K deviate from the predictions [7, 11]. In going from 300 K to 20 K, broad-range band structures up to -3 eV are strongly modified, which is consistent with the optical study [11]. The broad-range spectral change is more clearly seen in the energy distribution curves for 300 K and 20 K shown in Figs. 2(c) and (d), respectively. In going from 300 K to 20 K, spectral peaks at 300 K tend to be split into several structures probably due to complicated Jahn-Teller-like effect and band folding effect due to the charge and orbital ordering with the $(1/5, 0, -1/5)$ superstructure. Consequently, in the energy range from -0.2 eV to -3 eV, the spectral peaks at 20 K are much broader than those at 300 K.

On the other hand, spectral peaks from E_F to -0.2 eV are rather sharp at 20 K compared to those at 300 K as shown in Fig. 3. For 300 K, the outer hole band is indicated by the dashed curve in Fig. 3(a) which form the flower-shaped outer Fermi surface of Fig. 1(a). The inner hole-like band indicated by the dotted curves in Fig. 3(a) creates the hole pockets which corresponds to the inner Fermi surfaces of Fig. 1(a). By comparing between Figs. 3(a) and (b), while the outer band at 300 K is observed

separately from the inner one, the outer band at 20 K disappears near E_F . Across the transition, the outer band is shifted towards the inner one in this momentum region and is probably gapped due to the interaction with the inner band. This is consistent with the partial disappearance of the outer Fermi surface in Fig. 1(c). The inner hole-like band at 300 K is also strongly affected by the structural transition. The band located around ~ -0.15 eV of the A point at 300 K disappears at 20 K probably because it is shifted above E_F . Consequently, the hole band indicated by the dotted curve in Fig. 3(b) crosses E_F at 20 K and form the straight portions of the Fermi surfaces of Fig. 1(b). Such band reconstruction cannot be explained by a simple band folding picture, indicating orbital reconstruction by Jahn-Teller-like effect.

The Fermi surface mapping around the A point at 20 K is shown in Fig. 4(a). In general, straight Fermi surfaces with nesting wave vector q are expected to be gapped due to density wave formation with q . In IrTe₂, instead of gap opening, spectral weight at E_F is partially suppressed at specific points of the straight Fermi surfaces. In cuts 1 and 3 along the A-H direction [Figs. 4(b) and (d)], the hole band clearly crosses E_F and the spectral weight at E_F is not suppressed. On the other hand, in cut 2 [Fig. 4(c)], the intensity of the hole band is suppressed near E_F as seen in the EDC plot of Fig. 4(e). There are four points where the spectral weight at E_F is suppressed as seen in Fig. 4(a). Such spectral weight suppression at the specific points (cold spots) would be related to the origin of the superstructure of bulk IrTe₂ since the wave vectors connecting the two cold spots [indicated by the arrows in Fig. 4(a)] are approximately 2/5 of the A-L distance or 1/5 of the L-L' distance, partly consistent with its period. However, the partial spectral weight suppression would be due to surface effect or transition-matrix element effect, and no decisive conclusion can be obtained at the present stage. Here, it should be noted that the observed Fermi surfaces correspond to one of the Brillouin zone boundaries for possible domains. However, the crystal structure of low temperature phase is highly controversial (refs. 7, 11, and 13), and that, at the present stage, it is difficult to discuss relationship between the observed Fermi surfaces and the band folding due to the superstructure.

In conclusion, above the transition temperature, the observed Fermi surfaces and band dispersions are consistent with the band structure calculations. The flower-shaped outer Fermi surface (hole character) with six-fold symmetry and the inner Fermi surfaces (hole pockets) are observed. Across the structural transition, the geometry

of the inner Fermi surfaces is strongly modified. In the distorted phase, the inner Fermi surfaces consist of two straight portions, suggesting that nesting character is enhanced. However, the gap opening expected for CDW is not observed in the ARPES spectra, consistent with the optical study. Also the electronic structure up to ~ -3 eV is reconstructed by the lattice distortion, which is also consistent with the optical study. In addition, the spectral weight at E_F is suppressed at the specific points of the straight Fermi surfaces, which would be related to the origin of the superstructure.

The authors would like to thank valuable discussions with D. I. Khomskii and H. Takagi. This work was partially supported by a Grants-in-Aid for Young Scientists (B) (23740274, 24740238) from the Japan Society of the Promotion of Science (JSPS) and the Funding Program for World-Leading Innovative R&D on Science and Technology (FIRST Program) from JSPS. The synchrotron radiation experiment was performed with the approval of HSRC (Proposal No.12-A-12).

-
- [1] M. Imada, A. Fujimori, Y. Tokura: *Rev. Mod. Phys.* **70** (1998) 1039.
 - [2] S. Nagata, T. Hagino, Y. Seki, and T. Bitoh: *Physica B* **194 – 196** (1994) 1077.
 - [3] P. G. Radaelli, Y. Horibe, M. J. Gutmann, H. Ishibashi, C. H. Chen, R. M. Ibberson, Y. Koyama, Y. S. Hor, V. Kirykhin, and S. W. Cheong: *Nature* **416** (2002) 155.
 - [4] S. Nakatsuji and Y. Maeno: *Phys. Rev. Lett.* **84**, 2666 (2000).
 - [5] Y. Kamihara, T. Watanabe, M. Hirano, and H. Hosono: *J. Am. Chem. Soc.* **130** (2008) 3296.
 - [6] S. Pyon, K. Kudo, and M. Nohara: *J. Phys. Soc. Jpn.* **81** (2012) 053701.
 - [7] J. J. Yang, Y. J. Choi, Y. S. Oh, A. Hogan, Y. Horibe, K. Kim, B. I. Min, and S-W. Cheong: *Phys. Rev. Lett.* **108** (2012) 116402.
 - [8] N. Matsumoto, K. Taniguchi, R. Endoh, H. Takano, and S. Nagata: *J. Low Temp. Phys.* **117** (1999) 1129.
 - [9] D. I. Khomskii and T. Mizokawa: *Phys. Rev. Lett.* **94** (2005) 156402.
 - [10] D. Ootsuki, Y. Wakisaka, S. Pyon, K. Kudo, M. Nohara, M. Arita, H. Anzai, H. Namatame, M. Taniguchi, N. L. Saini, and T. Mizokawa: *Phys. Rev. B* **86** (2012) 014519.
 - [11] A. F. Fang, G. Xu, T. Dong, P. Zheng, and N. L. Wang: *Scientific Reports* **3** (2013) 1153.
 - [12] S. Pyon, K. Kudo, and M. Nohara: *Physica C* (2013)(in press) [DOI:10.1016/j.physc.2013.04.055].
 - [13] H. B. Cao, B. C. Chakoumakos, J. -Q. Yan, H. D. Zhou, R. Custelcean, and D. Mandrus: arXiv:1302.5369v1